# MOVPE Growth of LWIR AlInAs/GaInAs/InP Quantum Cascade Lasers: Impact of Growth and Material Quality on Laser Performance

Christine A. Wang, Benedikt Schwarz, Dominic F. Siriani, *Member, IEEE*, Leo J. Missaggia, Michael K. Connors, Tobias S. Mansuripur, Daniel R. Calawa, Daniel McNulty, Michael Nickerson, Joseph P. Donnelly, *Life Fellow, IEEE*, Kevin Creedon, and Federico Capasso, *Life Fellow, IEEE*

*(Invited Paper)*

***Abstract*—The quality of epitaxial layers in quantum cascade lasers (QCLs) has a primary impact on QCL performance, and establishing correlations between epitaxial growth and materials properties is of critical importance for continuing improvements. We present an overview of the growth challenges of these complex QCL structures; describe the metalorganic vapor phase epitaxy growth of AlInAs/GaInAs/InP QCL materials; discuss materials properties that impact QCL performance; and investigate various QCL structure modifications and their effects on QCL performance. We demonstrate uncoated buried-heterostructure 9.3-$\mu$m QCLs with 1.32-W continuous-wave output power and maximum wall plug efficiency (WPE) of 6.8%. This WPE is more than 50% greater than previously reported WPEs for unstrained QCLs emitting at 8.9 $\mu$m and only 30% below strained QCLs emitting around 9.2 $\mu$m.**

***Index Terms*—Semiconductor epitaxial layers, quantum effect semiconductor devices semiconductor lasers.**

## I. Introduction

QUANTUM cascade lasers (QCLs) [1] are compact coherent optical sources that emit over a wide wavelength range in the mid- to long-infrared (3–25 $\mu$m) as well as into part of the terahertz spectrum. With recent developments of AlInAs/GaInAs/InP QCLs exhibiting watt-class output power levels at room temperature in the mid-wave infrared (MWIR, 3–7 $\mu$m) and long-wave infrared (LWIR, 8–12 $\mu$m) regions, QCLs have become increasingly attractive for a number of technological applications including infrared (IR) countermeasures, free-space communications, and chemical and biological sensing.

As interest in QCLs continues to grow, so does the desire to improve performance and understand factors that may ultimately limit these unique and complex devices [2], [3]. QCLs are unipolar devices based on tunneling and intersubband transitions between quantum-confined energy states in the conduction band of a coupled quantum-well structure. These structures, designed using band structure engineering to optimize optical transitions and electron transport, consist of a complex sequence of barrier and quantum well layers with thicknesses ranging between 0.6 to 6 nm. Many hundreds of ultra-thin layers must be grown over microns of thickness, and thus it is not surprising that even though intersubband transitions for radiation amplification was proposed in 1971 [4], it was over 20 years before QCLs operating at cryogenic temperatures were first demonstrated in 1994 [1], and eight years later in 2002 for room temperature continuous-wave (cw) operation [5].

Exacting epitaxial growth of the QCL structure goes hand-in-hand with optimization of band-structure and wavefunction modeling, advanced processing involving fabrication and epitaxial regrowth of high-aspect ratio devices, and demanding heat-sinking packaging. Impressive progress has been made in each of these areas and QCLs with improved output power, operating temperature, wavelength range, and efficiency are routinely possible. Record performance at room temperature is 5 W cw output power and 21% wall plug efficiency (WPE) in the MWIR [6] and 2 W cw power and 10% WPE in the LWIR [7]. Those QCLs were grown by molecular beam epitaxy (MBE) or gas-source MBE, which are both high-vacuum growth processes. Another viable growth technique for QCLs is metalorganic vapor phase epitaxy (MOVPE), which operates at or slightly below atmospheric pressure. It is the mainstream

Manuscript received February 6, 2017; revised February 27, 2017; accepted February 28, 2017. Date of publication March 3, 2017; date of current version April 27, 2017. This work was supported by the Assistant Secretary of Defense for Research and Engineering under Air Force Contract FA8721-05-C-0002 and/or FA8702-15D-0001. The work of B. Schwarz was supported by the Austrian Science Funds within the project NanoPlas (P28914-N27).

C. A. Wang, L. J. Missaggia, M. K. Connors, D. R. Calawa, D. McNulty, M. Nickerson, J. P. Donnelly, and K. Creedon are with MIT Lincoln Laboratory, Lexington, MA 02420 USA (e-mail: wang@ll.mit.edu; missaggia@ll.mit.edu; connors@ll.mit.edu; calawa@ll.mit.edu; mcnulty@ll.mit.edu; michael.nickerson@ll.mit.edu; donnelly@ll.mit.edu; kevin.creedon@ll.mit.edu).

B. Schwarz was with the School of Engineering and Applied Sciences, Harvard University, Cambridge, MA 01238 USA. He is now with the Institute of Solid State Electronics, TU-Wien, Vienna 1040, Austria (e-mail: Benedikt.schwarz@tuwien.ac.at).

D. F. Siriani was with the MIT Lincoln Laboratory, Lexington, MA 02420 USA. He is now with Cisco Systems, Allentown, PA 18195 USA (e-mail: dsiriani@cisco.com).

T. S. Mansuripur was with the School of Engineering and Applied Sciences, Harvard University, Cambridge, MA 01238 USA. He is now with Pendar Technologies, Cambridge, MA 02138 USA (e-mail: tmansuripur@pendar.tech).

F. Capasso is with the School of Engineering and Applied Sciences, Harvard University, Cambridge, MA 01238 USA (e-mail: capasso@seas.harvard.edu).

Color versions of one or more of the figures in this paper are available online at http://ieeexplore.ieee.org.

Digital Object Identifier 10.1109/JSTQE.2017.2677899

platform for more conventional p-n optoelectronic devices and was shown to be suitable for QCL growth in the early 2000's [8]–[10]. Comparable performance between MOVPE [11] and MBE-grown QCLs [12] was demonstrated in 2006, although the QCL structures were different. Subsequently, numerous groups have pursued MOVPE for QCLs, and have achieved a high level of success [13]–[32].

In spite of these notable accomplishments, the epitaxial growth of QCL structures continues to be a challenge. In particular, the emission wavelength from QCLs of the same structure can not only be different when grown by MBE and MOVPE, but also different when grown by MOVPE at different organizations. For example, QCLs grown by MBE emitted at 9.3 $\mu$m [33], whereas QCLs grown by MOVPE from two different groups emitted at 8.4 $\mu$m [34] or at 9.2 $\mu$m [35]. QCLs of that same structure grown at our organization emitted around 10 $\mu$m. Thus, it is highly critical to clarify the origin of this discrepancy in order for MOVPE to be a more predictable growth technology.

This paper reviews the relationships between MOVPE growth of AlInAs/GaInAs/InP heterostructures, their materials properties, and QCL device performance, mainly focusing on unstrained LWIR QCLs. An overview of growth challenges is followed by the characterization of QCL materials and our recent results investigating the sensitivity of thickness variations and heterointerface grading on QCL performance. We have determined that while growth surfaces may be atomically abrupt, heterointerfaces are compositionally graded. Nonetheless, we will show that it is possible to adequately account for this grading in QCL bandstructure modeling and demonstrate that QCLs can be grown with wavelengths that are within 0.1 $\mu$m of calculated values. Furthermore, we demonstrate a record WPE of 6.8% for unstrained QCLs operating continuous wave at 9.3 $\mu$m. This WPE is more than 50% greater than the previously reported 4% WPE for unstrained QCLs emitting at 8.9 $\mu$m [36].

## II. AlInAs/GaInAs/InP QCL Materials Challenges

QCL structures are one of the most challenging semiconductor devices to grow in that they require precise control of alloy compositions, layer thicknesses, heterointerface quality, and doping of thick ($\sim$8–10 $\mu$m) structures composed of hundreds of ultrathin epilayers. Fig. 1 schematically shows the conduction band and wavefunctions of a QCL structure, and cross-section views of a buried heterostructure (BH) QCL and transmission electron microscopy (TEM) from a region of the QCL core. The QCL core typically consists of $\sim$600–1000 AlInAs barrier and GaInAs well layers, with thicknesses ranging between 0.6 to 6 nm, and thickness being specified to precision of 0.1 nm. To put this in perspective, one monolayer of the material (lattice matched to the InP substrate) is 0.293 nm. Thus, sub-monolayer thickness control is necessary if QCLs are to be grown according to design specifications. Alloy composition of AlInAs barriers and GaInAs wells should also be accurately controlled to replicate energy levels and band offsets that are specified in QCL bandstructure calculations, and to maintain structures that are overall lattice matched to the InP substrate. However, thickness precision is a more sensitive parameter than alloy composition.

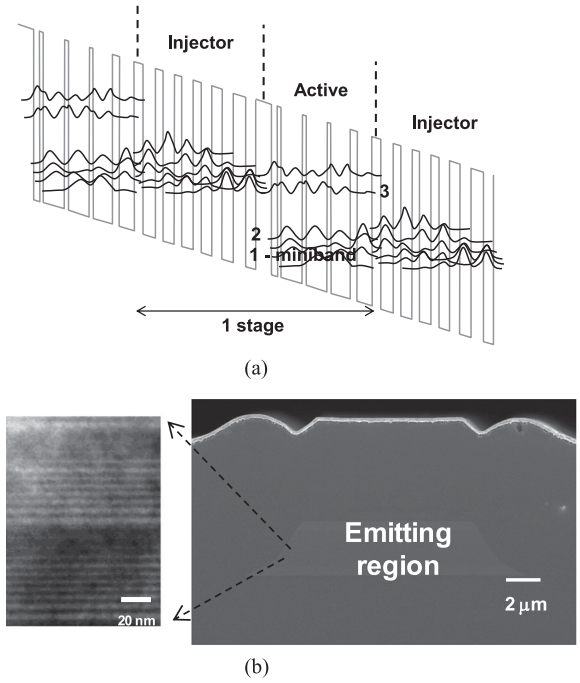


Fig. 1. (a) Conduction band diagram and wavefunctions of injector/active/injector region of 5-well single-phonon continuum QCL structure (after [15]). Laser action occurs between levels 3 and 2. The electron relaxes to the lower miniband, which transports it to the next period. One QCL stage consists of the injector and active region, and a full QCL structure typically has 30–40 stages. (b) Cross-section scanning electron micrograph of buried heterostructure QCL (right) and cross-section transmission electron micrograph of a portion of the QCL core.

Sub-nanometer variations in epitaxial thickness strongly alter energy levels and band alignments, and consequently, optical transition energies and QCL operating characteristics such as threshold currents and slope efficiency could be negatively affected.

QCLs can utilize AlInAs and GaInAs alloys lattice matched (LM) to the InP substrate, or strain-compensated (SC) layers in which AlnAs barriers in tension are strain compensated by GaInAs wells in compression. LM alloys are commonly used for LWIR QCLs while SC heterostructures, which provide increased conduction band offset to reduce carrier leakage, are necessary for high-performance MWIR QCLs [37] and beneficial for improving the WPE of LWIR QCLs [7], [38]. Strained layers further complicate the growth process because the strain introduces additional surface energy that can lead to strain-induced composition modulation and ultimately surface roughening, loss of periodicity, and ultimately defect generation [39]–[41]. Another important factor affecting QCL performance is interface roughness at barrier/well heterointerfaces. It leads to variations in thicknesses of barrier and well layers and results in increased interface roughness scattering and lower intersubband lifetimes, intersubband broadening and reduced gain [42]–[45]. Ideally, then heterointerfaces should be without interface roughness.

In practice, whether MBE or MOVPE is used, the epitaxial surface exhibits steps and interface roughness. At best, steps are only one monolayer high; step edges are straight; and MOVPE

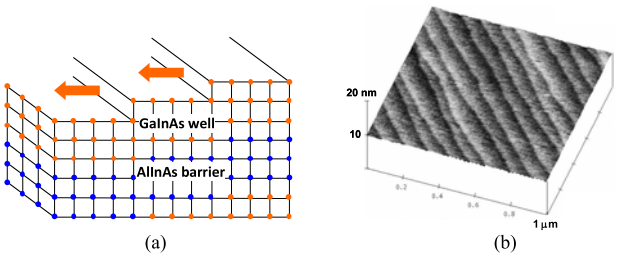


Fig. 2. (a) Schematic of crystal surface during epitaxial growth and (b) atomic force microscope image of epilayer surface with monolayer step heights and 'straight' step edges.

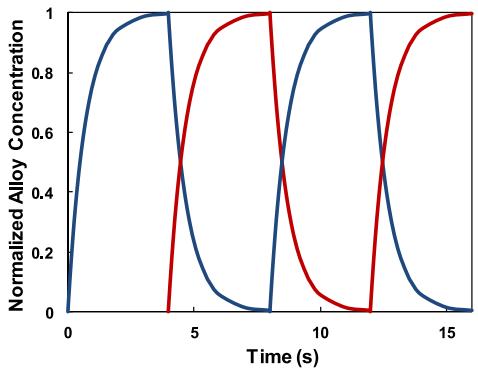


Fig. 3. Schematic precursor concentration profiles at the epilayer surface as a function of time for MOVPE growth. The grading is due to a fundamental phenomenon of gas phase dispersion operative in this growth process. Reducing the growth rate and the introduction of a growth interrupt between layers will reduce compositional grading at heterointerfaces.

growth advances in a step-flow mode as illustrated in Fig. 2. The step width is determined by the miscut angle of the InP substrate, provided that growth conditions result in a step-flow mode, and is associated with a correlation length. Since intersubband scattering times depend on the correlation length [45], the miscut angle may be an important consideration for QCLs in the absence of interface roughness due to other types of growth perturbations.

Another materials consideration is the compositional profile of heterointerfaces. In MBE, heterointerfaces are compositionally abrupt by virtue of growth taking place in high-vacuum and the use of shutters in front of effusion cells. However, in MOVPE, heterostructure composition profiles depend on precursor gas residence times in the reactor. Gas dispersion is a fundamental phenomenon in the MOVPE process, and smears out the compositional gas front. As a result, rather than having an abrupt compositional step change at the wafer surface, the profile exhibits a transient before reaching a steady state value as schematically shown in Fig. 3 [46], [47]. The time required to reach the steady-state concentration depends on gas residence time. These times are influenced by the gas handling system, reactor geometry, and growth process parameters. Gas systems and reactors have been engineered to minimize residence times, and growth parameters might be further adjusted to minimize interfacial grading via growth at low-pressure and increased carrier gas flow rates, reduced epilayer growth rate, and addition of a growth interruption at each heterointerface. Indeed, in the early years of developing MOVPE-grown QCLs, it was shown that QCL performance was better with lower growth rates and the incorporation of a growth interrupt [10], [17].

Another fundamental phenomenon that will impact both MBE and MOVPE materials is indium surface segregation, whereby an indium-rich region tends to form at the growing surface [48], [49]. Indium surface segregation has been observed in both MBE [48], [50]–[52], specially designed QCL structures grown by MBE [53], and MOVPE [26], [54]. Indium segregation leads to interface broadening where both interface roughness and alloy grading are observed. Segregation lengths of 2.9 nm are reported for MBE-grown GaInAs/GaInAs quantum wells [51]; ∼1.2 nm for MBE-grown AlInAs/GaInAs QCL structures [53]; and ∼2.5–4.5 nm for MOVPE-grown AlInAs/GaInAs quantum wells [26], [54].

The extent of interface roughness and grading due to indium segregation will depend on parameters such as growth temperature, growth rate, V/III ratio, and growth interruptions. Nonetheless, indium segregation introduces interface roughness, and as discussed above, it can impact QCL performance, including emission wavelength. Anecdotally, it is interesting to note that the full-width at half-maximum (FWHM) value of electroluminescence (EL) spectrum from MBE-grown SC QCLs was lower than that from MOVPE-grown material (26.3 vs 32.7 meV) [36], [55].

As discussed, growth of QCL materials presents numerous challenges whether grown by MBE, GSMBE, or MOVPE. Fortunately, progress in our understanding of these materials continues to be made, and better correlations between QCL materials and device performance can be established.

## III. Growth and Characterization of QCLs

AlInAs/GaInAs/InP QCL materials have been grown by MOVPE in a variety of reactors, including horizontal and vertical geometries, research and production machines, and single- or multi-wafer reactors. Growth occurs at low pressures to minimize heterointerface alloy grading [46], [47]. Typical precursors are trimethylaluminum (TMAl), trimethylgallium (TMGa) or triethlygallium (TEGa), and trimethylindium (TMIn) as group III precursors; phosphine and arsine as group V precursors; and $SiH_4$ or $Si_2H_6$ as the n-type dopant [8], [10], [35], [56]–[59]. Alternative group V sources, tertiarybutylphosphine (TBP) and tertiarybutylarsine (TBAs), pyrolize at lower temperatures than phosphine or arsine and were used for SC alloys, since strain-induced surface roughening is reduced at lower growth temperatures [19], [20]. Reported growth parameters are: temperatures ∼600–725 °C; low growth rates 0.1–0.3 nm/s for QCL core structures and higher growth rates ∼0.5–1.0 nm/s for waveguide and cladding layers; and V/III ratios as low as 5 for alternative group V precursors and 20–350 for hydride precursors. The growth space is extremely wide, and optimization of materials can only be established through an iterative process of materials growth and a variety of characterization techniques.

It is important to be able to not only characterize the materials on an atomic scale, but also on the macroscopic scale since the laser gain originates from a ∼2–3$\mu$m thick QCL core

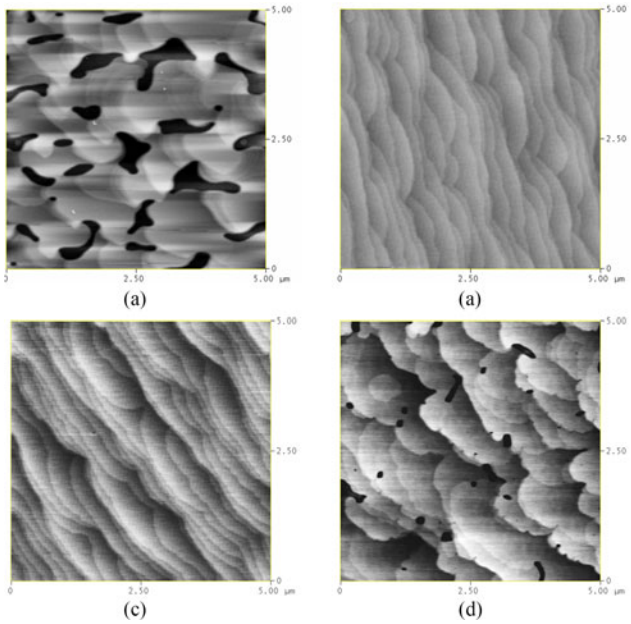


Fig. 4. (a) Atomic force microscopy (AFM) images ($5 \times 5\ \mu m^2$) illustrate the high sensitivity of surface morphology to growth conditions. AFM images are for AlInAs grown at 580 °C with tertiarybutylarsine and different growth rates (GR) or V/III ratios: (a) $\mathrm{GR} = 0.15$ nm/s ($\mathrm{V/III} = 5$), (b) $\mathrm{GR} = 0.28$ nm/s ($\mathrm{V/III} = 5$), (c) $\mathrm{V/III} = 2.5$ ($\mathrm{GR} = 0.26$ nm/s), and (d) $\mathrm{V/III} = 20$ ($\mathrm{GR} = 0.26$ nm/s). The root-mean-square roughness of the surfaces shown (a)–(d) are 2.3, 0.175, 0.276, and 0.588 nm, respectively. From [19].

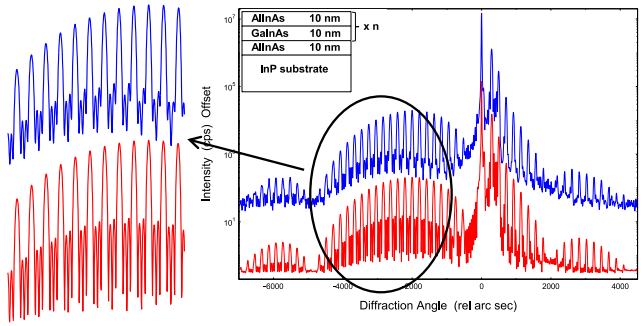


Fig. 5. High-resolution x-ray diffraction scans of an AlInAs/GaInAs multiple quantum well. Upper curve is the measured data, and the lower curve is a simulation using Philips X'pert software (PANalytical Inc.). Alloy compositions are determined from the angular position and thickness from angular spacing. The full-width at half-maximum (FWHM) of satellite diffraction peaks and interference fringes between satellites are a measure of the overall material quality. The narrow FWHM of measured scans indicate consistent periodicity from the initially grown layers to the uppermost surface.

that consists of tens of periods of ultrathin layers. The materials properties of interest include surface morphology, alloy composition, structural, electrical, and optical properties, as well as heterointerface quality. These properties are similar to what is required for most semiconductor devices, and the use of complementary characterization methods used in concert is especially powerful in providing insights for optimizing growth. Ultimately, though, correlation with QCL device performance is required to complete the cycle for optimization. Both in-situ and ex-situ techniques are used to characterize QCL materials, and while the focus here is on MOVPE-grown structures, results from MBE-grown QCLs are discussed when relevant.

Overall surface morphology is examined with Nomarski contrast microscopy and can be further optimized on the atomic scale by using atomic force microscopy (AFM) to examine the evolving growth surface. This assumes, of course, that the growth surface does not undergo significant changes as the wafer is cooled down from the growth temperature. As shown in Fig. 2, the best surfaces for QCLs have monolayer step heights and smooth step edges. Achieving those surfaces, however, is challenging and sensitively dependent on epitaxial growth conditions [19], [20], [35]. Fig. 4 shows an example of AFM images from AlInAs layers that were grown at different V/III ratios and growth rates [19]. The surface step structure is highly sensitive to relatively small changes in these parameters. The example shown here is for layers grown with TBAs, for which growth temperatures and V/III ratios are different from those for AlInAs layers grown with arsine, but the intent is to illustrate the marked changes in surface step structure on growth parameters. Alloys containing different elements have fundamentally different thermodynamics and kinetics, and therefore each alloy used as constituent layers in the QCLs should be optimized. It was observed that AlInAs is more sensitive to growth conditions than GaInAs [19], [35]. We attribute this to the lower surface mobility of Al compared to Ga. On the other hand, the highly mobile indium atom provides a larger operating window for step-flow growth of InP (see Fig. 2). The width of the surface steps is dependent on substrate miscut angle, which is another parameter that can affect surface morphology [35] and ultimately the interface roughness.

High-resolution x-ray diffraction (HRXRD) and structure simulation are extremely critical and integral components in the development of QCL materials. AlInAs and GaInAs alloy compositions and growth rates must be determined with a high level of accuracy for QCL growth. From HRXRD rocking curves, the alloy composition, thickness, and overall quality can be determined by comparing measured scans with simulations. Furthermore, HRXRD is highly sensitive in evaluating overall MQW structural and heterointerface quality. The approach is illustrated and described in Fig. 5. The full-width at half-maximum (FWHM) of satellite diffraction peaks is related to the perfection of periodicity of the entire structure. Note that sharp satellites are not necessarily indicative of interface abruptness, but rather that the transition between barrier and well layers, even if it is graded, is highly reproducible from growth of the first to final period. Furthermore, when measured FWHM values are the same as simulated values, the heterointerfaces very likely are atomically smooth.

When composition and thickness are determined from bulk ($\sim$0.3–0.4 $\mu$m thick) epilayers, and this information is used for QCL growth, it is often observed that the QCL period and overall lattice matching deviate considerably from the expected values. Therefore, additional refinement of the growth rate and alloy calibration is performed by growing a series of AlInAs/GaInAs multiple quantum well (MQW) structures with varying barrier and well layer thicknesses; using HRXRD to determine the MQW period (from angular separation between satellite

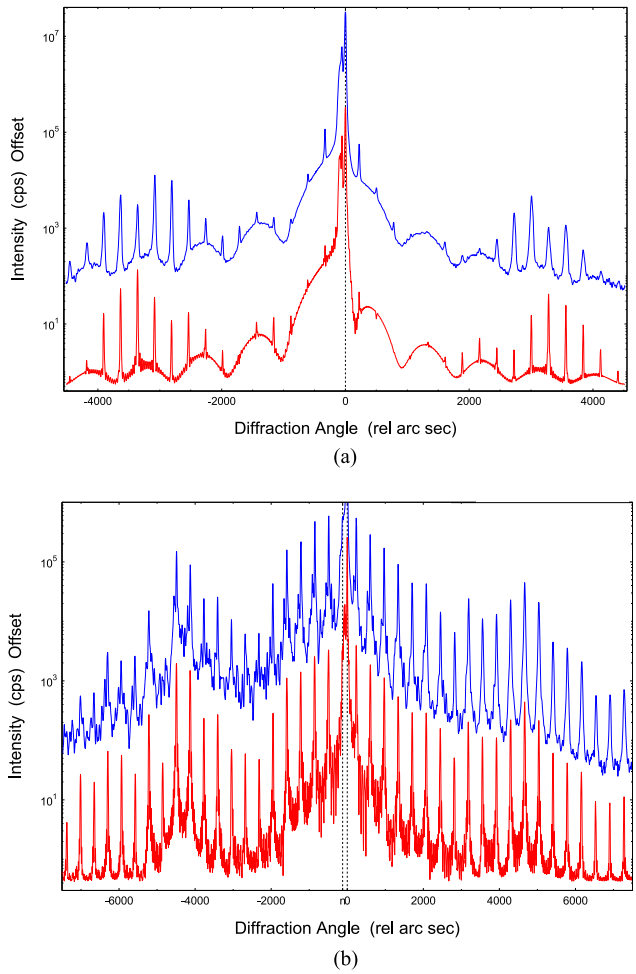


Fig. 6. High-resolution x-ray diffraction scans (upper) and simulations (lower) of full QCL structures. (a) Lattice-matched (LM) LWIR QCL and (b) strain-compensated (SC) MWIR QCL (from [59] and [19], respectively). The diffraction contrast is much larger for SC QCLs, and the regularly space satellite peaks are related to the QCL period.

diffraction peaks); and performing a linear regression analysis. Examples of HRXRD scans for LM and SC QCLs are shown in Fig. 6.

While HRXRD is an indispensible tool and is sufficient to characterize structures for QCL growth, it only provides the overall information of the total layer structure and no microscopic details of individual layers. Further probing of structures on the atomic scale can be done using a number of techniques. Cross-section TEM can be used to image individual barrier and well layers via contrast differences, and thus thickness variations and interface roughness can be evaluated [35], [58], [60]. Cross-section scanning-tunnelling microscopy provides exquisite quantitative chemical information on the atomic scale, and was used to study heterointerfaces in MBE-grown QCLs. It was found that indium segregation occurs across AlInAs and GaInAs layers and leads to graded layers of about 4 monolayers [53].

High-angle annular dark-field (HAADF) scanning TEM (STEM) is highly sensitive to atomic number and when used in conjunction with energy-dispersive x-ray spectroscopy, can yield quantitative composition profiles on an atomic scale. In a recent report, the Al composition and layer thickness profiles in MOVPE-grown QCL structures were calculated from intensity profiles of HAADF STEM images [61]. It was found that many of the barrier layers are AlGaInAs quaternaries instead of AlInAs. Furthermore, thinner barrier layers had lower Al content than thicker ones. To correct the Al profiles, higher Al precursor flows were used for a subsequent QCL growth, and the emission wavelength of those lasers blue shifted from 9.3 to 8.4 $\mu$m, compared to the nominal design wavelength of 8.9 $\mu$m.

A technique that can map chemical information on a 3-dimensional atomic spatial scale is atom probe tomography (APT) [62]. Results from a 2-dimensional analysis of a MOVPE-grown AlInAs/GaInAs MQW test structure revealed that Al, Ga, and In profiles were graded over 2.5–4.5 nm [26]. Data also showed an InAs-rich AlGaInAs interfacial layer due to indium segregation. This grading and segregation are particularly important for the very narrow barrier and well layers as it leads to lower effective barrier heights and lower barrier strength, effectively resulting in red-shifted QCL emission wavelengths [26].

A subtlety of the AlInAs/GaInAs heterointerface is that the interfaces are not symmetric. Based on adatom surface mobility considerations, interface roughness at the GaInAs-on-AlInAs interface is expected to be rougher than at the AlInAs-on-GaInAs interface. The effect of interface roughness and growth direction on QCLs was investigated by designing and growing symmetric devices, that is, they could be operated with either bias polarity [63], [64]. Experimental results show a definitive preference for bias, and demonstrate the large impact of interface roughness on QCL performance. In designing QCLs, it may also be important to consider whether the QCL structure uses a vertical or diagonal laser transition, the former being less sensitive to interface roughness [45], [65].

Doping concentration in the QCL active region affects the dynamical operating range [66]–[69]. Once a minimum concentration level is introduced so as to provide sufficient gain, increasing the doping level results in a small penalty to threshold current density ($J_{th}$) but large increase in maximum current density ($J_{max}$) where maximum power is attained. In the range where band bending effects, impurity scattering, and free-carrier absorption can be neglected, $J_{max}$ scales linearly with doping, and the laser's dynamic operating range is increased. However, above an upper limit, $J_{max}$ and slope efficiency degrade [68]. Typically, the range over which lasing can be achieved is only about half a decade at a sheet density of around $1 \times 10^{11}$ cm$^{-2}$. However, the doping level has been shown to also depend on the background doping in the MBE growth chamber [67]. Thus, to establish the optimum injector doping, several QCLs with different doping levels should be grown and lasing performance evaluated. The high sensitivity of background doping and intentional doping of the active region on QCL performance may explain the performance variability that has been reported for established processes within the same organization [28], [70], but this is only speculation because limited information is available.

Background impurities can be measured by secondary ion mass spectroscopy. Impurities of interest are Si, O, and C. Si and C are typically at low levels $<10^{16}$ cm$^{-3}$ and relatively

insensitive to growth conditions. O levels in AlInAs depend on growth temperature, decreasing as the temperature is increased. On the other hand, the O level in GaInAs is insensitive to temperature [35]. O is a deep level in AlInAs and while QCLs are unipolar devices and not impacted by electron-hole non-radiative recombination, it is still advantageous to minimize O levels as the O can degrade surface morphology.

All the above mentioned characterization methods are ex-situ measurements of completed structures. In order to track epitaxial growth in real time, it is highly desirable to have in-situ optical monitoring on the reactor. Near normal spectral reflectance is sensitive to refractive index material changes [71] and is the most commonly used in-situ monitoring approach for MOVPE. With multiple wavelength reflection, it is possible to obtain real-time information of the growth rate, alloy compositions, heterointerface switching, and surface roughening. Furthermore, wafer curvature that evolves due to layer strain can be continuously monitored [72]–[75]. In-situ monitoring is a tremendous aid in troubleshooting and identifying where epitaxial growth may have gone awry. Since the growth time for QCLs is typically 5–10 hours long depending on growth rates, in-situ monitoring can save hours if a run needs to be prematurely terminated. Once a growth process has been established, the in-situ reflectance serves as a 'fingerprint' of the growth runs and is extremely useful for tracking growth reproducibility over time. Perhaps an equally important aspect of in-situ monitoring, providing it is stable and a database of temperature dependent refractive indices is available, is that the numerous calibrations needed to grow QCLs can be executed in a few (if not single) growth run.

## IV. LWIR QCLs

### A. Growth and Processing

AlInAs/GaInAs/InP QCLs were grown on (1 0 0) n-InP substrates by MOVPE in a Veeco D125 multi-wafer (3 × 2) reactor with 28 slpm $H_2$ as the carrier gas and reactor pressure of 60 Torr. TMAl, TMGa, and TMIn were used for group III precursors, and phosphine and arsine as group V precursors. $Si_2H_6$ (diluted 200 ppm in H2) was used as the n-type dopant. The growth temperature was 625 °C as measured by emissivity corrected optical pyrometry. AlInAs and GaInAs were grown with a single TMIn source. The growth rate of both alloys was ∼0.3 nm/s, and no growth interrupt was used between AlInAs and GaInAs interfaces. InP layers were grown at a higher rate of 0.6–0.7 nm/s. The V/III ratios were ∼ 90 for AlInAs and GaInAs, and ∼ 130 for InP. Epilayer structures were grown nominally lattice matched to the (1 0 0) n-InP substrates, doped 2–5 × $10^{18}$ $cm^{-3}$.

A QCL structure based on single-phonon continuum depopulation was adopted as the baseline structure for this study, as this scheme was designed to be robust against layer-thickness fluctuations [14] and has been shown to result in high performance [15]. The reported design wavelength is 8.6 $\mu$m. The injector/active region is composed of nominally LM AlInAs/GaInAs. The layer sequence in nm of one period starting from the injection barrier is as follows: **3.8**/1.5/**0.9**/5.3/**0.8**/5.2/**0.9**/4.8/**1.6**/3.7/**2.2**/3.0/**1.8**/2.8/**1.9**/2.7/**2.0**/2.6/**2.5**/2.7/**3.1**/2.5. The AlInAs barrier layers are in bold print, and the underlined layers are Si-doped injector layers. The injector doping ranged from 8 × $10^{10}$ to 1.4 × $10^{11}$ $cm^{-2}$. Thirty five periods were grown for all structures. The lower and upper InP cladding layer thickness was 3.5 $\mu$m, and was Si doped 5 × $10^{16}$ $cm^{-3}$. GaInAs waveguide layers were Si doped 2 × $10^{16}$ $cm^{-3}$ and were 0.5 $\mu$m thick. The heavily Si-doped (5 × $10^{16}$ $cm^3$) InP plasma-confinement layer was 0.5 $\mu$m thick, followed by a 0.02 $\mu$m-thick heavily Si doped (>2 × $10^{19}$ $cm^{-3}$) GaInAs contact layer.

QCL structures were fabricated as mesas and ridge lasers by using conventional photolithography and wet etching processes. Following wet etching, the side-walls were electrically insulated with a 0.3 $\mu$m-thick $Si_3N_4$ dielectric layer. Ti-Au metallization was used for top contact, the wafer thinned, and the bottom Ti-Au contact deposited. The ridge lasers are either 20 or 25 $\mu$m in width. Lasers were cleaved into 3-mm-long bars and the facets were left uncoated.

For demonstration of cw operation, buried heterostructures (BH) were fabricated. A $Si_3N_4/Al_2O_3$ mask was patterned with 12 $\mu$m ridges aligned along [1 1 0]. A combination of dry and wet etching was used to form the ridges. Just prior to regrowth, the sample was lightly etched in a bromine based etch, HBr:Br saturated $H_2O$:$H_2O$ (1:1:10), which has been shown to minimize electrically active impurities at the regrowth interface [76], and immediately loaded into the reactor. Fe-InP was selectively grown to planarize the ridges. After regrowth, the mask was removed and the top Ti-Au metallization formed, followed by substrate thinning, back contact metallization, and cleaving. QCLs were bonded epilayer side down on Cu submounts with In solder [25].

Uncoated wet-etched QCLs were probe tested in chip form without additional mounting. For cw operation, packaged QCLs were tested with water cooling at 15 °C. Pulsed laser testing was performed under low-duty factor pulsed conditions, 200 ns at a repetition frequency of 1 kHz. Laser power was coupled into an integrating sphere with HgCdTe detector (Vigo PCI-3TE-12). Power calibration of the photodetector signal was made by measuring the laser power using a thermal detector. The lasing wavelength was measured using a Fourier-transform infrared spectrometer.

### B. Effect of Thickness Variations

Reproducible growth of QCL structures requires stable reactor conditions over long periods of time. In practice, growth rates can drift over time. It is also possible that the growth rate is miscalculated, since individual barrier and well rates are calculated from the total MQW, and thus these rates could slightly compensate each other. To investigate the effects of potential thickness variabilities on QCL performance, the baseline QCL was grown with intentionally varied layer thicknesses [77]. Either the period thickness was changed ∼ ±4% or complementary thickness changes were made (increase in barrier with decrease in well) of ±0.5 or ±1.0 Å were made. The injector doping was 8 × $10^{10}$ $cm^{-2}$.

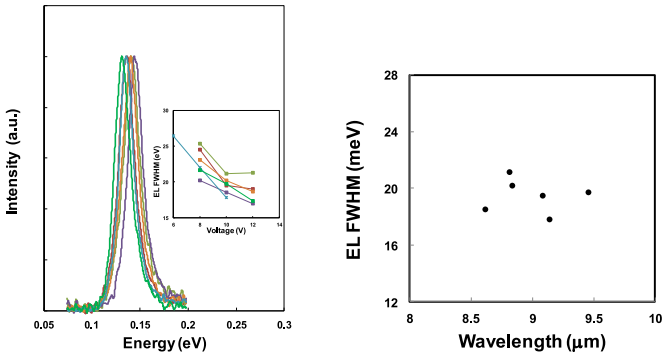


(a) (b)

Fig. 7. To investigate sensitivity of thickness changes on QCL performance, single-phonon-continuum QCL structures were grown with either period or complementary thickness (increasing barrier/decreasing well) changes to QCL active/injector layers. (a) Electroluminescence (EL) spectra is from round mesa structures measured at 10 V. The inset shows the dependence of EL linewidth on voltage. From [77]. (b) EL full-width at half-maximum (FWHM) as a function of wavelength.

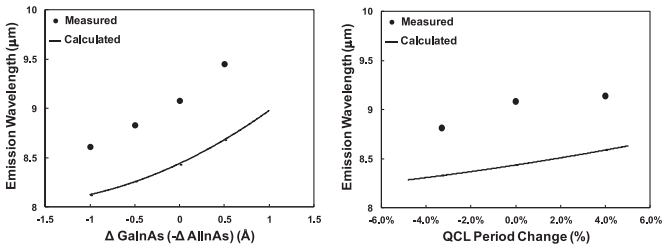


(a) (b)

Fig. 8. Electroluminescence emission wavelength for QCL structures grown with either (a) complementary barrier/well thickness changes or (b) QCL period changes. The calculated data assumes compositionally abrupt interfaces. Complementary thickness changes have a significantly larger impact on wavelength than overall period changes.

Fig. 7(a) shows the EL spectra for round mesas measured at 10 V and Fig. 7(b) shows the EL FWHM as a function of wavelength. The emission wavelength spans over a wide range from 8.6 to 9.5 $\mu$m, while EL FWHM values are in a narrow range from 17.8 to 21.2 meV. No trend with wavelength is observed over this range. Assuming that the material quality such as interface roughness is not the cause of the FWHM variation, it is more probable that the variation is related to the thickness changes that alter energy levels in the QCL structure, and thus carrier transport. All these FWHM values are smaller compared to the value of 22.3 meV reported for the same structure grown by MOVPE [15]. Our EL FWHM data are consistent with QCL structures with high crystal quality, low background impurity levels, and low interface roughness.

The measured wavelength data versus thickness change are compared to calculated values and summarized in Fig. 8. The trend in experimental wavelength change with thickness is consistent with predicted trends, but there is about a 0.6 $\mu$m red shift of measured data compared to the model. This shift is attributed to compositionally graded interfaces [26]. These results are consistent with other reports related to grading of heterointerfaces in AlGaAs/GaAs QCLs. Unintentional or intentional grading was associated with a red-shifted emission wavelength

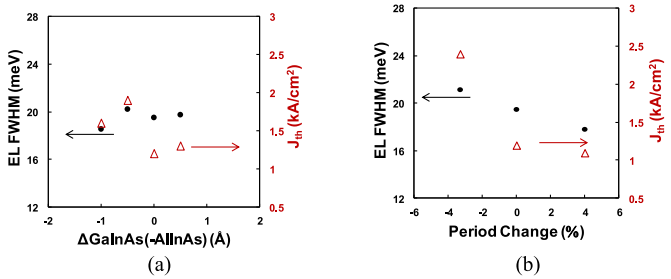


(a) (b)

Fig. 9. Electroluminescence spectra full-width at half-maximum (EL FWHM) and threshold current density ($J_{th}$) for QCL structures grown with either (a) complementary barrier/well thickness changes or (b) QCL period changes. EL FWHM data are represented by closed circles and $J_{th}$ by open red triangles. Reducing the GaInAs well thickness slightly increases $J_{th}$, while a smaller QCL period is more detribmental to QCL performance than increasing the period.

[9], [78], [79]. Perhaps a more interesting observation is that the strength of the wavelength shift with thickness depends on the type of variation. The change in emission wavelength with QCL period is $<$40 nm/% period change. On the other hand, complementary thickness changes have a larger effect, causing a shift of $>$500 nm/0.1 nm. It is thus unlikely that the large differences between emission wavelengths reported for MOVPE-grown QCLs is due to the QCL period change [10].

The difference in the strength of wavelength variation with thickness can qualitatively be explained by the change in energy splitting of both isolated single-well states and super-states from coupling of single-well states. The mean position of the group of upper and lower active region states is about equal to the energy of the second and first energy level of an isolated well, respectively. In general, the energy splitting of individual well states is determined by well thickness and splitting of super-states in each group by barrier thickness. The upper laser state is generally the bottommost state of the upper active region group, and the lower laser state is the topmost of the lower active region group; their separation is about equal to the energy splitting between lower and upper well states minus the amount they are moved up (lower state) and down (upper state) from the mean position by coupling splitting. Thus, when both wells and barriers are made thicker, the effects tend to cancel, keeping the net splitting relatively small. In contrast, when wells and barriers are changed complementarily, the effects move the laser energy states in opposite directions, increasing or decreasing energy splitting depending on the well or barrier thickness change. Although this type of analysis has not been applied to other QCL designs, similar effects are expected in different QCL structures, and further studies are necessary to confirm the phenomenon and to quantify its magnitude.

QCL ridges, 25 $\mu$m $\times$ 3 mm, were measured under pulsed conditions and the threshold current densities ($J_{th}$) and corresponding EL FWHM are shown in Fig. 9 for the different thickness changes. For complementary thickness changes, Fig. 9(a), $J_{th}$ is lowest at 1.2 kA/cm$^2$ for no thickness changes and increases to 1.6–1.9 kA/cm$^2$ for structures with thinner GaInAs wells. The slightly lower $J_{th}$ value of 1.6 kA/cm$^2$ for complementary thickness changes of $-1$ Å GaInAs/ 1 Å AlInAs compared to 1.9 kA/cm$^2$ for $-0.5$ Å GaInAs/ 0.5 Å AlInAs may

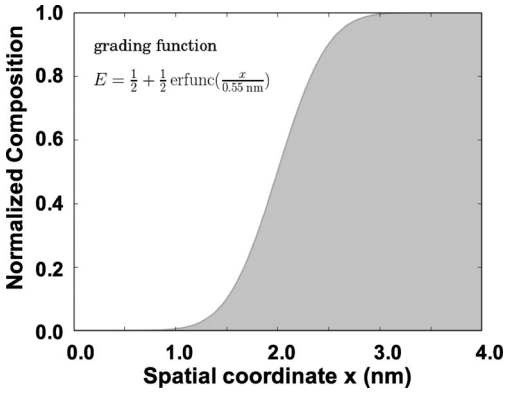


Fig. 10. Normalized composition profile of graded heterointerface used in bandstructure calculations.

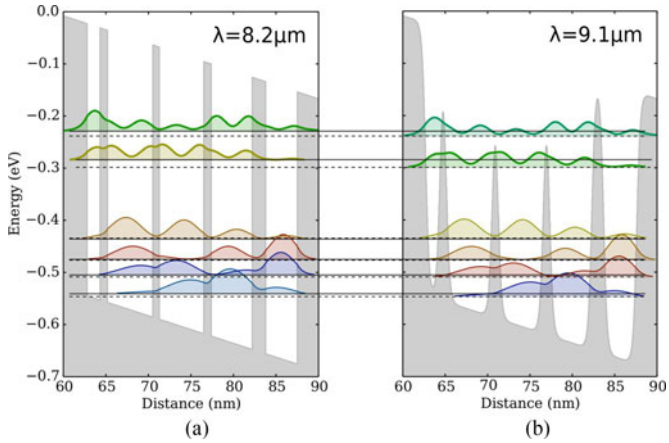


Fig 11. Calculated conduction band diagram and moduli squared of the wave functions for the active region of the QCL with compositionally (a) abrupt interfaces (8.2 $\mu$m lasing transition) and (b) graded interfaces (9.1 $\mu$m lasing transition). The barrier heights of the three thinner barrier layers are considerably lower and consequently the lasing transition energy is reduced by 15 meV. From [26].

be related to an observed larger QCL period of the former QCL, which was 5% larger than intended. More significant changes in $J_{th}$ are measured for QCL period changes, Fig. 9(b). The lowest measured $J_{th}$ is 1.1 kA/cm$^2$ for the QCL with a 4% increased period, but $J_{th}$ increased to 2.4 kA/cm$^2$ for the QCL with 3.3% smaller period. The slope efficiency was statistically insensitive to complementary changes, while it increased slightly from 1.3 to 1.4 W/A when the period was increased from the nominal value by 4%. A possible explanation for these results is related to the thinnest wells, which are located in the injector and coupling well of the active region, and are particularly important for carrier transport. If heterointerfaces are graded, the wells would be shallower than desirable and impede carrier transport.

### C. Bandstructure Modeling of Graded Interfaces

As it has become clear that AlInAs/GaInAs heterointerfaces are compositionally graded in our MOVPE-grown QCL structures, QCLs were modeled to account for these graded interfaces [26]. Bandstructure simulations are based on the Vienna Schrödinger Poisson framework [80]. As an approximation and to first establish the method, a relatively simple model was adopted to represent intermixing between AlInAs and GaInAs. The graded interface results in the quaternary alloy AlGaInAs, where the interfacial layer between lattice-matched GaInAs and AlInAs can be described by the function $1/(1+\exp(\mathrm{x/L}))$, where L is the grading width. A barrier has the concentration shape $1/(1+\exp((\mathrm{x}-\mathrm{dB})/\mathrm{L})) - 1/(1+\exp(\mathrm{x/L}))$. Using in-house historically measured QCL electroluminescence wavelengths, L was empirically determined to be 0.22 nm. Alternatively, the grading can be described by the error function $1/2 + 1/2\,\mathrm{erf}\,(\mathrm{x/L})$ and the barrier concentration by ½ [erf(x/L) – erf ((x-dB)/L)], with L = 0.55 nm. Both descriptions of the concentration profile yield similar profiles as expected [81], and the normalized composition profile for the error function is shown in Fig. 10.

The same baseline QCL structure described above was used in bandstructure simulations. Fig. 11(a) and (b) show the bandstructure and moduli squared of the wavefunctions in the active region in which the barrier and well layers are compositionally abrupt or graded, respectively. The grading causes a dramatic change in the alloy composition and energy levels in the active region, where the three barrier layers have the quaternary AlGaInAs composition. The calculated transition energy for the QCL with abrupt interfaces corresponds to a wavelength of 8.2 $\mu$m (which differs from the reported value of 8.6 $\mu$m for this structure [15], and could be due to different bandstructure parameters used in their model). With graded interfaces resulting in AlGaInAs instead of AlInAs barriers, energy barrier heights are lower and consequently the lasing transition energy is reduced by 15 meV, or equivalently to a lasing wavelength of 9.1 $\mu$m. These results clearly illustrate the large impact that graded AlInAs/GaInAs heterointerfaces can have on the QCL emission wavelength.

QCLs were designed for emission at 7.5 and 8.5 $\mu$m and the bandstructures and wavefunctions are shown in Fig. 12. It is possible that graded interfaces could lead to performance degradation, depending on the extent of grading and if not considered in the design. Since the barrier layers in the gain section of a QCL are the thinnest, they are the most affected by graded interfaces. QCLs are commonly designed with multiple extractor levels matched to the LO-phonon energy. The grading leads to a stronger splitting of these levels, which can lead to a slightly higher lower-laser-level lifetime. The extent of the subband energy level changes strongly depends on the barrier and well thickness and is thus very different in the gain section and the injector. Thus the injection efficiency into the upper laser level might be impaired due to a misalignment. Furthermore, grading of the thin barrier layers leads to a reduction of the effective barrier height, which may lead to a higher escape probability to the continuum. Note also that the thinnest GaInAs well is shallower which slightly misaligns energy levels. On the other hand, the SPC QCL design used in this study is very robust and specifically designed to be less sensitive to growth non-idealities [15].

We also looked into alternative approaches to fit the experimental emission wavelengths, e.g. using modified band-parameters or changing the well/barrier ratio. Although we were

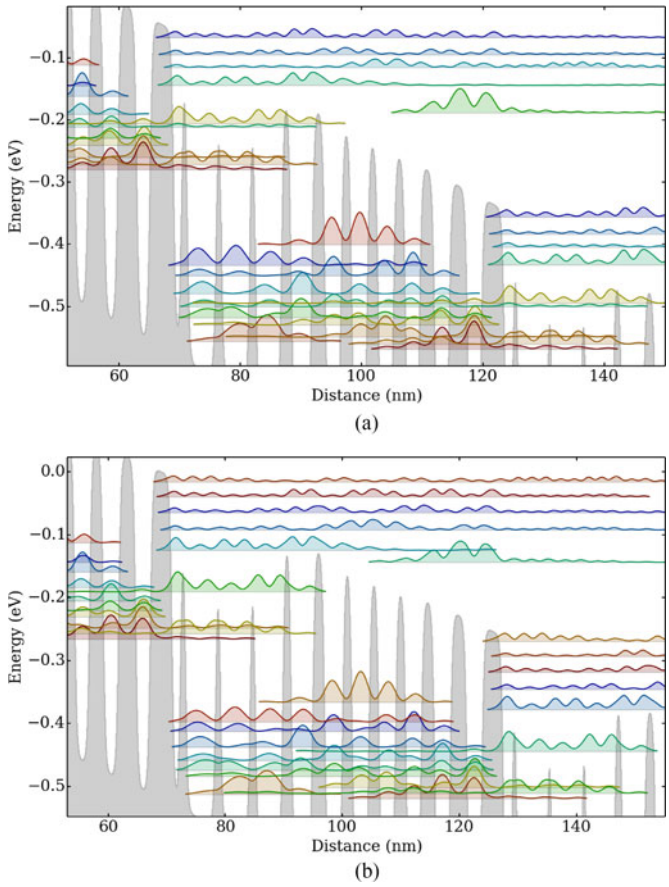


Fig. 12. Calculated conduction band diagram and moduli squared of the wave functions for QCLs designed for (a) 7.5 $\mu$m and (b) 8.5 $\mu$m emission. The AlInAs/GaInAs layer sequence in nm of one period starting from the injection barrier is as follows: (a) **4.1**/1.1/**1.1**/4.65/**0.95**/4.55/**1.05**/4.2/**1.7**/3.3/**2.3**/2.5/**1.9**/2.4/**2.0**/2.3/**2.2**/2.1/**2.7**/2.15/**3.3**/2.0 and (b) **3.9**/1.3/**0.95**/5.1/**0.85**/5.0/**0.95**/4.6/**1.6**/3.5/**2.2**/2.9/**1.8**/2.7/**1.9**/2.6/**2.0**/2.4/**2.5**/2.45/**3.1**/2.3. The AlInAs barrier layers are in bold print, and the underlined layers are Si-doped injector layers. From [26].

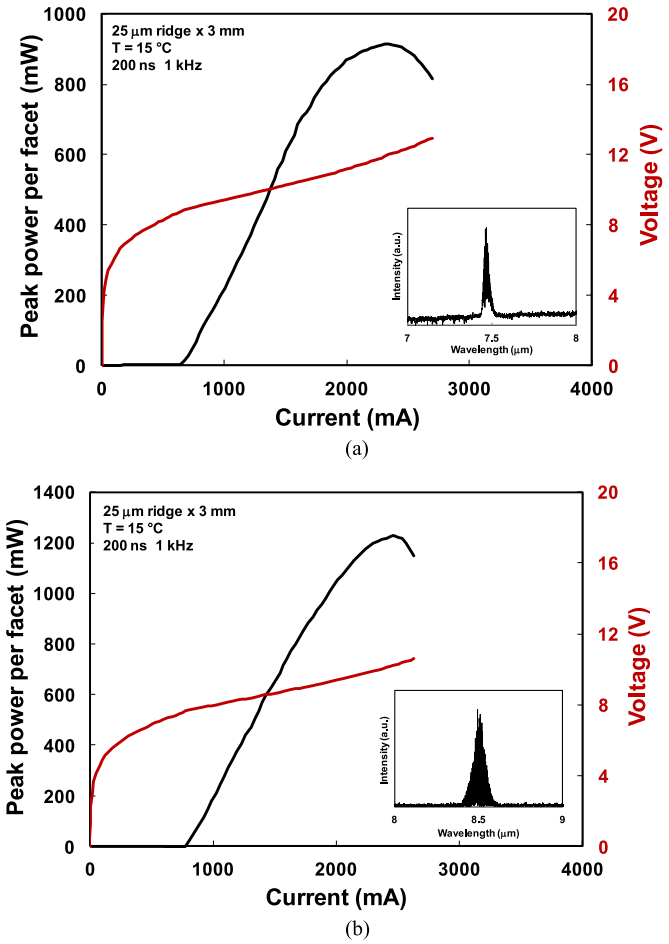


Fig. 13. Pulsed mode power operation of probe-tested uncoated QCLs designed with graded interfaces: (a) 7.5 $\mu$m design and (b) 8.5 $\mu$m design. The inset shows the emission spectrum measured just above threshold. The injector doping level was $1.1 \times 10^{11}$ cm$^{-2}$ for both designs, and was not optimized. The 7.5 $\mu$m laser has a threshold current density $J_{th}$ of 0.85 kA/cm$^2$, 1.8 W total peak output power, total slope efficiency of 1.6 W/A, and maximum total power conversion efficiency $\eta_{max}$ of 8.2%. The 8.5 $\mu$m laser has a slightly higher threshold current density $J_{th}$ of 1.1 kA/cm$^2$, nearly 2.5 W total peak power, total slope efficiency of 1.8 W/A, and maximum total power conversion efficiency $\eta_{max}$ of 11%. From [26].

able to fit the wavelengths of similar designs, we did not find a single parameter set to fit our entire set of test QCL structures. Only the graded interface model allowed predicting the wavelengths of all samples within a reasonable accuracy of $+-0.05$–$0.1$ $\mu$m. One has to note, that fitting the wavelength is not sufficient to prove correctness, but it can give a hint. Only the gain section of a QCL determines the wavelength, but also the injector section is relevant for its performance. In the injector section the well/barrier ratio, as well as their thicknesses are different relative to the gain section. As a consequence, fitting the three different models to the wavelength leads to different injector subband structures. We believe that the graded interface model closer represents the reality, which was also confirmed by APT and thus is favorable. In the case of smaller interface grading widths, the other models might be an alternative. We also tried to improve the grading model by using different shapes for both interface types and one of them considering a longer tail similar to APT data. However, the resulting parameter space becomes unpractical and would require a rigorous study in order to add additional value.

### *D. QCL Devices*

To evaluate the predictability of this model with graded interfaces, QCLs with the design shown in Fig. 12 for emission at 7.5 and 8.5 $\mu$m were grown with 35 periods and injector sheet doping of $\sim 1.1 \times 10^{11}$ cm$^{-2}$ and same waveguide structure described above. The injector doping was not optimized. Pulsed light-current (L-I) and voltage-current (V–I) characteristics of the uncoated QCL devices (25 $\mu$m $\times$ 3 mm-long) are shown in Fig. 13 with insets showing the lasing spectra. The 7.5 $\mu$m laser has a threshold current density $J_{th}$ of 0.85 kA/cm$^2$, 1.8 W total peak output power, total slope efficiency of 1.6 W/A, and maximum total power conversion efficiency $\eta_{max}$ of 8.2%. The 8.5 $\mu$m laser has a slightly higher threshold current density $J_{th}$ of 1.1 kA/cm$^2$, nearly 2.5 W total peak power, total slope efficiency of 1.8 W/A, and maximum total power conversion efficiency $\eta_{max}$ of 11%. The lasing wavelengths of these devices are 7.46 and 8.5 $\mu$m measured just past threshold and are very well

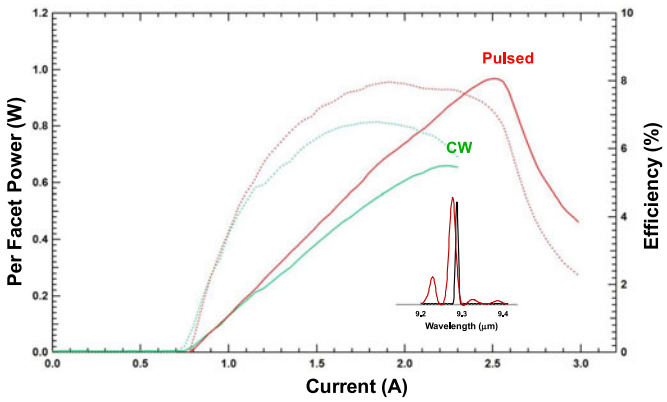


Fig. 14. Pulsed and continuous-wave operation of a 9.3-$\mu$m uncoated buried-heterostructure QCL (12 $\mu$m $\times$ 5 mm-long) measured at 15 °C. For pulsed and cw operation, the maximum total power is 1.94 and 1.32 W, and maximum WPE is 8 and 6.8%, respectively. Total slope efficiency is 1.4 and 1.2 W/A for pulsed and cw operation, respectively.

correlated with the design wavelengths. Another QCL designed for 8.0 $\mu$m emission had a measured emission wavelength of 8.0 $\mu$m, and similar high performance with $J_{th} \sim 1.1$ kA/cm$^2$, 2 W/A, and $\eta_{max} = 9.4\%$. The excellent agreement between measured and calculated QCL wavelengths validates the modeling approach to account for graded interfaces.

For cw operation, 9.3-$\mu$m QCLs were processed as BH QCLs with a 12-$\mu$m wide mask. As fabricated BH ridges were 14 $\mu$m wide, and cleaved into 5 mm long bars. The QCL structure was the baseline structure with 35 periods with no modifications. Fig. 14 shows the optical power and conversion efficiency versus current for water cooling temperature of 15 °C. For pulsed and cw operation, the maximum total power is 1.94 and 1.32 W, and maximum WPE is 8 and 6.8%, respectively. Total slope efficiency is 1.4 and 1.2 W/A for pulsed and cw operation, respectively. The ratio of pulsed/cw power is only 1.5, and is indicative of good thermal performance for this design (the $T_0$ was reported to be 201 K) as well as efficient heat removal from the active region with the BH and packaging. This high cw WPE exceeds the value of 2.7% that was reported for the same structure grown by MOVPE [15]. Indeed, the highest WPE previously reported is 4% for unstrained QCLs emitting at 8.9 $\mu$m [70], and 10% for strained QCLs at 9 $\mu$m [7]. These results are evidence that even with graded interfaces, state-of-the-art QCL performance can be achieved.

The grading has its largest impact on the narrow barriers in the gain section and leads to an effective reduction of their height. Interestingly, the obtained situation looks similar to designs that use multiple strained compositions, although the barriers are shallower. Using strained material to increase the band-offset is an efficient method to realize QCLs at shorter wavelength but also to increase the injection efficiency of LWIR QCLs [6], [7], [37], [82]. We expect that our designs can be further improved by increasing barrier heights that follow the gain section via strain management.

In order to project the cw operation from our wet-etched QCLs emitting at 7.5–8.5 $\mu$m, we compare the cw performance of the 9.3-$\mu$m BH QCLs to our unmounted uncoated wet-etched QCLs from the same wafer used for processing BH QCLs. For wet-etched devices, $J_{th}$, total slope efficiency, and power conversion efficiency were 1.1 kA/cm$^2$, 1.4 W/A, and 8.6%, respectively. These values are very close to those measured for the pulsed performance of packaged BH QCLs. Therefore, we expect that cw operation for the7.5–8.5 $\mu$m QCLs can be estimated by scaling the performance of wet-etched devices. Further tests are needed to statistically confirm this correlation, but initial experiments are consistent with this approach. Furthermore, fully packaged BH quantum cascade laser/detectors emitting at 8.0 $\mu$m, also unstrained materials, have cw WPE of 7% [32].

## V. Conclusions

The material quality in QCLs has a primary impact on QCL operation, and this paper discusses correlations between the MOVPE growth of QCL heterostructures, their materials properties, and QCL performance. We demonstrate the importance of having detailed characterization on both the macroscopic as well as on the atomic scale to use as input for QCL bandstructure modeling. We investigated various QCL structure modifications and their affects on QCL performance. Compared to calculated emission wavelengths, our QCLs are red shifted 0.6 $\mu$m. Materials studies revealed that heterointerfaces are compositionally graded as a result of the fundamental nature of AlInAs/GaInAs materials, as well as the MOVPE growth process. Therefore, to better model MOVPE-grown QCLs, band structure and wavefunction calculations were made with graded heterointerface profiles. Unstrained QCLs were designed and fabricated for emission between 7.5 and 8.5 $\mu$m. QCLs emit within 0.1 $\mu$m of the designed wavelength, demonstrating the importance of having detailed knowledge of QCL materials. These QCLs exhibit room-temperature peak powers exceeding 1.8 W and efficiencies of $\sim$ 8 to 10% for 25 $\mu$m $\times$ 3 mm ridge devices. Furthermore, buried heterostructure QCLs emitting at 9.3 $\mu$m operate cw with output power 1.32 W with WPE of $\sim 6.8\%$. This WPE is more than 50% greater than previously reported WPEs for unstrained QCLs and only 30% below strained QCLs emitting in this wavelength range. This work shows that even with compositionally graded heterointerfaces, QCLs can yield state-of-the-art performance.

## Acknowledgment

Any opinions, findings, conclusions or recommendations expressed in this material are those of the authors and do not necessarily reflect the views of the Assistant Secretary of Defense for Research and Engineering.

## References

[1] J. Faist *et al.*, "Quantum cascade laser," *Science*, vol. 264, pp. 553–556, 1994.
[2] J. Faist, "Wallplug efficiency of quantum cascade lasers: Critical parameters and fundamental limits," *Appl. Phys. Lett.*, vol. 90, 2007, Art. no. 253512.
[3] Q. K. Yang *et al.*, "Wall-plug efficiency of mid-infrared quantum cascade lasers," *J. Appl. Phys.*, vol. 111, 2012, Art. no. 053111.
[4] R. F. Kazarinov and R. A. Suris, "Possibility of the amplification of electromagnetic waves in a semiconductor with a superlattice," *Sov. Phys. Semicond.*, vol. 5, pp. 707–709, 1971.

[5] M. Beck *et al.*, "Continuous wave operation of a mid-infrared semiconductor laser at room temperature," *Science*, vol. 295, pp. 301–305, 2002.

[6] Y. Bai, N. Bandyopadhyay, S. Tsao, S. Slivken, and M. Razeghi, "Room temperature quantum cascade lasers with 27% wall plug efficiency," *Appl. Phys. Lett.*, vol. 98, 2011, Art. no. 181102.

[7] A. Lyakh, R. Maulini, A. Tsekoun, R. Go, and C. K. N. Patel, "Multiwatt long wavelength quantum cascade lasers based on high strain composition with 70% injection efficiency," *Opt. Express*, vol. 20, pp. 24272–24279, 2012.

[8] R. P. Green *et al.*, "Room-temperature operation of InGaAs/AlInAs quantum cascade lasers grown by metalorganic vapor phase epitaxy," *Appl. Phys. Lett.*, vol. 83, pp. 1921–1922, 2003.

[9] J. S. Roberts *et al.*, "Quantum cascade lasers grown by metalorganic vapor phase epitaxy," *Appl. Phys. Lett.*, vol. 82, pp. 4221–4223, 2003.

[10] D. Bour *et al.*, "Metalorganic vapor-phase epitaxy of room-temperature, low-threshold InGaAs/AlInAs quantum cascade lasers," *J. Cryst. Growth*, vol. 272, pp. 526–530, 2004.

[11] L. Diehl *et al.*, "Pulsed- and continuous-mode operation at high temperature of strained quantum-cascade lasers grown by metalorganic vapor phase epitaxy," *Appl. Phys. Lett.*, vol. 88, 2006, Art. no. 041102.

[12] A. Evans *et al.*, "High-temperature, high-power, continuous-wave operation of buried heterostructure quantum-cascade lasers," *Appl. Phys. Lett.*, vol. 84, pp. 314–316, 2004.

[13] X. J. Wang, J. Y. Fan, T. Tanbun-Ek, and F.-S. Choa, "Low threshold quantum-cascade lasers of room temperature continuous-wave operation grown by metal-organic chemical-vapor deposition," *Appl. Phys. Lett.*, vol. 90, 2007, Art. no. 211103.

[14] K. Fujita *et al.*, "Room temperature, continuous-wave operation of quantum cascade lasers with single phonon resonance-continuum depopulation structures grown by metal organic vapor-phase epitaxy," *Appl. Phys. Lett.*, vol. 91, 2007, Art. no. 141121.

[15] K. Fujita *et al.*, "High-performance $\lambda \sim 8.6$ $\mu$m quantum cascade lasers with single phonon-continuum depopulation structures," *IEEE J. Quantum Electron.*, vol. 46, no. 5, pp. 683–688, May 2010.

[16] K. Fujita, M. Yamanishi, S. Furuta, A. Sugiyama, and T. Edamura, "Extremely temperature-insensitive continuous-wave quantum cascade lasers," *Appl. Phys. Lett.*, vol. 101, 2012, Art. no. 181111.

[17] M. Troccoli *et al.*, "High-performance quantum cascade lasers grown by metal-organic vapor phase epitaxy and their applications to trace gas sensing," *J. Lightw. Technol.*, vol. 26, pp. 3534–3555, 2008.

[18] M. Troccoli, "High power emission and single mode operation of quantum cascade lasers for industrial applications," *IEEE J. Sel. Topics Quantum Electron.*, vol. 21, no. 6, Nov./Dec. 2015, Art. no. 1200207.

[19] C. A. Wang *et al.*, "OMVPE growth of highly strain-balanced GaInAs/AlInAs/InP for quantum cascade lasers," *J. Cryst. Growth*, vol. 310, pp. 5191–5197, 2008.

[20] C. A. Wang *et al.*, "Strain-compensated GaInAs/AlInAs/InP quantum cascade laser materials," *J. Cryst. Growth*, vol. 312, pp. 1157–1164, 2010.

[21] S. Menzel *et al.*, "Quantum cascade laser master-oscillator power-amplifier with 1.5 W output power at 300 K," *Opt. Express*, vol. 19, pp. 16229–16235, 2011.

[22] B. Gokden *et al.*, "High-brightness tapered quantum cascade lasers," *Appl. Phys. Lett.*, vol. 102, 2013, Art. no. 053503.

[23] P. Rauter *et al.*, "High-power arrays of quantum cascade laser master-oscillator power-amplifiers," *Opt. Express*, vol. 21, pp. 4518–4530, 2013.

[24] J. Montoya *et al.*, "Integration of quantum cascade lasers and passive waveguides," *Appl. Phys. Lett.*, vol. 107, 2015, Art. no. 031110.

[25] L. Missaggia *et al.*, "Thermal management of quantum cascade lasers in an individually addressable monolithic array architecture," *Proc. SPIE*, vol. 9730, 2016, Art. no. 973008.

[26] C. A. Wang *et al.*, "Sensitivity of heterointerfaces on emission wavelength of quantum cascade lasers," *J. Cryst. Growth*, vol. 464, pp. 215–220, 2017.

[27] F. Xie *et al.*, "Room temperature CW operation of short wavelength quantum cascade lasers made of strain balanced $Ga_xIn_{1-x}As$/AlInAs material on InP substrates," *IEEE J. Sel. Topics Quantum Electron.*, vol. 17, no. 5, pp. 1445–1452, Sep./Oct. 2011.

[28] F. Xie *et al.*, "Watt-level room temperature continuous-wave operation of quantum cascade lasers with $\lambda > 10$ $\mu$m," *IEEE J. Sel. Topics Quantum Electron.*, vol. 19, no. 4, Jul./Aug. 2013, Art. no. 1200407.

[29] J. D. Kirch *et al.*, "86% internal differential efficiency from 8 to 9 $\mu$m-emitting, step-taper active-region quantum cascade lasers," *Opt. Express*, vol. 24, pp. 24483–24494, 2016.

[30] J. D. Kirch *et al.*, "5.5 W near-diffraction-limited power from resonant leaky-wave coupled phase-locked arrays of quantum cascade lasers," *Appl. Phys. Lett.*, vol. 106, 2015, Art. no. 061113.

[31] J. D. Kirch *et al.*, "Highly temperature insensitive, low threshold-current density ($\lambda = 201$;8.7–8.8 $\mu$m) quantum cascade lasers," *Appl. Phys. Lett.*, vol. 106, 2015, Art. no. 151106.

[32] B. Schwarz *et al.*, "Watt-level continuous wave emission from a bi-functional quantum cascade laser/detector," *ACS Photonics*, to be published, doi: 10.1021/acsphotonics.7b00133.

[33] D. Hofstetter *et al.*, "Continuous wave operation of a 9.3 $\mu$m quantum cascade laser on a Peltier cooler," *Appl. Phys. Lett.*, vol. 78, pp. 1964–1966, 2001.

[34] L. Diehl *et al.*, "High-power quantum cascade lasers grown by low-pressure metal organic vapor-phase epitaxy operating in continuous wave above 400 K," *Appl. Phys. Lett.*, vol. 88, 2006, Art. no. 201115.

[35] Y. Huang *et al.*, "Optimization of growth conditions for InGaAs/InAlAs/InP quantum cascade lasers by metalorganic chemical vapor deposition," *J. Cryst. Growth*, vol. 316, pp. 75–80, 2011.

[36] M. Troccoli *et al.*, "Long-wave IR quantum cascade lasers for emission in the $\lambda = 8$–12 $\mu$m spectral region," *Opt. Mater. Express*, vol. 3, pp. 1546–1560, 2013.

[37] J. Faist *et al.*, "Short wavelength ($\lambda \sim 3.4$ $\mu$m) quantum cascade laser based on strained compensated InGaAs/AlInAs," *Appl. Phys. Lett.*, vol. 72, pp. 680–682, 1998.

[38] R. Maulini, A. Lyakh, A. Tsekoun, and C. K. N. Patel, "$\lambda \sim 7.1$ $\mu$m quantum cascade lasers with 19% wall-plug efficiency at room temperature," *Opt. Express*, vol. 19, pp. 17203–17211, 2011.

[39] A. Ponchet, A. Rocher, J.-Y. Emery, C. Starck, and L. Goldstein, "Lateral modulations in zero-net-strained GaInAsP multilayers grown by gas source molecular-beam epitaxy," *J. Appl. Phys.*, vol. 74, pp. 3778–3782, 1993.

[40] T. Tsuchiya, M. Komori, R. Tsuneta, and H. Kakibayashi, "Investigation of effect of strain-compensated structure and compensation limit in strained-layer multiple quantum wells," *J. Cryst. Growth*, vol. 145, pp. 371–375, 1994.

[41] P. Desjardins, H. Marchand, L. Isnard, and R. A. Masut, "Microstructure and strain relaxation in organometallic vapor phase epitaxy of strain-compensated GaInP/InAsP multilayers on InP(001)," *J. Appl. Phys.*, vol. 81, pp. 3501–3511, 1997.

[42] A. Wittmann, Y. Bonetti, J. Faist, E. Gini, and M. Giovannini, "Intersubband linewidths in quantum cascade laser designs," *Appl. Phys. Lett.*, vol. 93, 2008, Art. no. 141103.

[43] J. B. Khurgin *et al.*, "Role of interface roughness in the transport and lasing characteristics of quantum-cascade lasers," *Appl. Phys. Lett.*, vol. 94, 2009, Art. no. 091101.

[44] Y. Chiu *et al.*, "Importance of interface roughness induced intersubband scattering in mid-infrared quantum cascade lasers," *Appl. Phys. Lett.*, vol. 101, 2012, Art. no. 171117.

[45] A. Bismuto, R. Terazzi, M. Beck, and J. Faist, "Influence of the growth temperature on the performances of strain-balanced quantum cascade lasers," *Appl. Phys. Lett.*, vol. 98, 2011, Art. no. 091105.

[46] C. A. Wang, S. Patnaik, J. W. Caunt, and R. A. Brown, "Growth characteristics of a vertical rotating-disk OMVPE reactor," *J. Cryst. Growth*, vol. 93, pp. 228–234, 1988.

[47] S. Patnaik, R. A. Brown, and C. A. Wang, "Hydrodynamic dispersion in rotating-disk OMVPE reactors: Numerical simulation and experimental measurements," *J. Cryst. Growth*, vol. 96, pp. 153–174, 1989.

[48] J. M. Moison, C. Guille, F. Houzay, F. Barthe, and M. Van Rompay, "Surface segregation of third-column atoms in group III-V arsenide compounds: Ternary alloys and heterostructures," *Phys. Rev. B*, vol. 40, pp. 6149–6162, 1989.

[49] J.-M. Gerard, "In situ probing at the growth temperature of the surface composition of (InGa)As and (InAl)As," *Appl. Phys. Lett.*, vol. 61, pp. 2096–2098, 1992.

[50] J. M. Moison *et al.*, "Surface segregation in III-V alloys," *J. Cryst. Growth*, vol. 111, pp. 141–150, 1991.

[51] K. Muraki, S. Fukatsu, Y. Shiraki, and R. Ito, "Surface segregation of In atoms during molecular beam epitaxy and its influence on the energy levels in InGaAs/GaAs quantum wells," *Appl. Phys. Lett.*, vol. 61, pp. 557–559, 1992.

[52] G. Grenet, E. Bergignat, M. Gendry, M. Lapeyrade, and G. Hollinger, "In situ XPS investigation of indium surface segregation for $Ga_{1-x}In_xAs$ and $Al_{1-x}In_xAs$ alloys grown by MBE on InP(001)," *Surf. Sci.*, vol. 352–354, pp. 734–739, 1996.

[53] P. Offermans *et al.*, "Digital alloy interface grading of an InAlAs/InGaAs quantum cascade laser structure studied by cross-sectional scanning tunneling microscopy," *Appl. Phys. Lett.*, vol. 83, pp. 4131–4133, 2003.
[54] A. A. Marmalyuk *et al.*, "Investigation of indium segregation in InGaAs/(Al)GaAs quantum wells grown by MOCVD," *J. Cryst. Growth*, vol. 237–239, pp. 264–268, 2002.
[55] A. Lyakh *et al.*, "3 W continuous-wave room temperature single-facet emission from quantum cascade lasers based on nonresonant extraction design approach," *Appl. Phys. Lett.*, vol. 95, 2009, Art. no. 141113.
[56] F. Xie *et al.*, "High-temperature continuous-wave operation of low power consumption single-mode distributed-feedback quantum-cascade lasers at $\lambda \sim 5.2$ $\mu$m," *Appl. Phys. Lett.*, vol. 95, 2009, Art. no. 091110.
[57] J. C. Shin *et al.*, "Highly temperature insensitive, deep-well 4.8 $\mu$m emitting quantum cascade semiconductor lasers," *Appl. Phys. Lett.*, vol. 94, 2009, Art. no. 201103.
[58] J. C. Shin, L. J. Mawst, and D. Botez, "Crystal growth via metal–organic vapor phase epitaxy of quantum-cascade-laser structures composed of multiple alloy compositions," *J. Cryst. Growth*, vol. 357, pp. 15–19, 2012.
[59] C. A. Wang *et al.*, "High power ($>$5 W) $\lambda \sim 9.6$ $\mu$m tapered quantum cascade lasers grown by OMVPE," *J. Cryst. Growth*, vol. 370, pp. 212–216, 2013.
[60] J. Faist *et al.*, "High power mid-infrared quantum cascade lasers with a molecular beam epitaxy grown InP cladding operating above room temperature," *J. Cryst. Growth*, vol. 175/176, pp. 22–28, 1997.
[61] K. Pantzas *et al.*, "Sub-nanometrically resolved chemical mappings of quantum-cascade laser active regions," *Semicond. Sci. Technol.*, vol. 31, 2016, Art. no. 055017.
[62] T. F. Kelly and M. K. Miller, "Atom probe tomography," *Rev. Sci. Instrum.*, vol. 78, 2007, Art. no. 031101.
[63] C. Deutsch *et al.*, "Probing scattering mechanisms with symmetric quantum cascade lasers," *Opt. Express*, vol. 21, pp. 7209–7215, 2013.
[64] P. M. Bouzi *et al.*, "Importance of growth direction in mid-infrared quantum cascade lasers," *J. Appl. Phys.*, vol. 116, 2014, Art. no. 034504.
[65] J. Faist *et al.*, "Vertical transition quantum cascade laser with Bragg confined excited state," *Appl. Phys. Lett.*, vol. 66, pp. 538–540, 1995.
[66] M. Giehler *et al.*, "Lasing properties of GaAs/(Al,Ga)As quantum-cascade lasers as a function of injector doping density," *Appl. Phys. Lett.*, vol. 82, pp. 671–673, 2003.
[67] T. Aellen *et al.*, "Doping in quantum cascade lasers. I. InAlAs–InGaAs/InP midinfrared devices," *J. Appl. Phys.*, vol. 100, 2006, Art. no. 043101.
[68] C. Mann *et al.*, "Influence of injector doping concentration on the performance of InP-based quantum-cascade lasers," *IEEE J. Quantum Electron.*, vol. 42, no. 10, pp. 994–1000, Oct. 2006.
[69] E. Mujagic *et al.*, "Impact of doping on the performance of short-wavelength InP-based quantum-cascade lasers," *J. Appl. Phys.*, vol. 103, 2008, Art. no. 033104.
[70] M. Troccoli, X. Wang, and J. Fan, "Quantum cascade lasers: High-power emission and single-mode operation in the long-wave infrared ($\lambda >$ 6 $\mu$m)," *Opt. Eng.*, vol. 49, 2010, Art. no. 111106.
[71] W. G. Breiland and K. P. Killeen, "A virtual interface method for extracting growth rates and high temperature optical constants from thin semiconductor films using in situ normal incidence reflectance," *J. Appl. Phys.*, vol. 78, pp. 6726–6736, 1995.
[72] P. Wolfram, E. Steimetz, W. Ebert, N. Grote, and J. T. Zettler, "Routine growth of InP based device structures using process calibration with optical in-situ techniques," *J. Cryst. Growth*, vol. 272, pp. 118–124, 2004.
[73] F. Brunner *et al.*, "Growth optimization during III-nitride multiwafer MOVPE using real-time curvature, reflectance and true temperature measurements," *J. Cryst. Growth*, vol. 298, pp. 202–206, 2007.
[74] M. Sugiyama, K. Sugita, Y. Wang, and Y. Nakano, "In situ curvature monitoring for metal-organic vapor phase epitaxy of strain-balanced stacks of InGaAs/GaAsP multiple quantum wells," *J. Cryst. Growth*, vol. 315, pp. 1–4, 2011.
[75] S. Ma *et al.*, "Effect of hetero-interfaces on in situ wafer curvature behavior in InGaAs/GaAsP strain-balanced MQWs," *J. Cryst. Growth*, vol. 352, pp. 245–248, 2012.
[76] E. Yablonovitch, R. Bhat, C. E. Zah, T. J. Gmitter, and M. A. Koza, "Nearly ideal InP/$In_{0.53}Ga_{0.47}As$ heterojunction regrowth on chemically prepared $In_{0.53}Ga_{0.47}As$ surfaces," *Appl. Phys. Lett.*, vol. 60, pp. 371–373, 1992.
[77] D. F. Siriani *et al.*, "Sensitivity of quantum cascade laser performance to thickness and doping variations," *J. Cryst. Growth*, vol. 452, pp. 263–267, 2016.
[78] S. Anders, W. Schrenk, T. Roch, C. Pflügl, and G. Strasser, "Tuning quantum-cascade lasers by postgrowth rapid thermal processing," *Appl. Phys. Lett.*, vol. 84, pp. 164–166, 2004.
[79] T. Roch, C. Pflügl, A. M. Andrews, W. Schrenk, and G. Strasser, "X-ray investigation of quantum well intermixing after postgrowth rapid thermal processing," *J. Phys. D: Appl. Phys.*, vol. 38, pp. A132–A136, 2005.
[80] O. Baumgartner, Z. Stanojevic, and H. Kosina, *Monte Carlo Methods and Applications*, vol. 59. Borovets, Bulgaria: De Gruyter, 2012.
[81] X. Lü, L. Schrottke, E. Luna, and H. T. Grahn, "Efficient simulation of the impact of interface grading on the transport and optical properties of semiconductor heterostructures," *Appl. Phys. Lett.*, vol. 104, 2014, Art. no. 232106.
[82] D. Botez, C.-C. Chang, and L. J. Mawst, "Temperature sensitivity of the electro-optical characteristics for mid-infrared ($\lambda =$ 3-16 $\mu$m)-emitting quantum cascade lasers," *J. Phys. D.: Appl. Phys.*, vol. 49, 2016, Art. no. 043001.

**Christine A. Wang** received the S.B., M.S., and Ph.D. degrees from the Massachusetts Institute of Technology, in 1977, 1978, and 1984, respectively. She is a Senior Staff Member in the Laser Technology and Applications Group, Lincoln Laboratory, Massachusetts Institute of Technology, where she has worked since joining in 1984. She has authored or coauthored more than 170 publications, has seven patents, one patent pending, and edited one book. Her research interest focuses on the growth, characterization, and optimization of epitaxial III–V semiconductors for optoelectronic devices. Dr. Wang is a member of the National Academy of Inventors.

**Benedikt Schwarz** received the M.Sc. degree in microelectronics with honors from TU Wien in 2011, investigating quantum effects, discrete dopants and oxide traps in nanoscaled MOS transistors. His graduation was honored by the Austrian Federal Ministry of Science and Research. He received the Ph.D. degree in 2015, developing a monolithically integrated lab-on-a-chip using quantum cascade technology and was awarded by the European technology platform Photonics21 for innovative research and by INITs business incubator for its high commercial potential. He visited the Capasso lab at Harvard University in March–June 2015 and June 2016 and is currently a Researcher and Project Leader at TU Wien. His current research interest includes nanoplasmonics, quantum cascade devices, frequency combs, nonlinear optics, chemical sensing, near-field optical microscopy and 2-D materials.

**Dominic F. Siriani** (S'07–M'11) received the B.S., M.S., and Ph.D. degrees in electrical engineering from the University of Illinois at Urbana-Champaign in 2006, 2007, and 2011, respectively. During his graduate studies, he researched photonic crystal VCSELs and coherently coupled antiguided VCSEL arrays. In 2011, he joined the technical staff in Lincoln Laboratory, Massachusetts Institute of Technology, where he was with the Laser Technology and Applications Group. He is currently working on semiconductor lasers at Cisco Systems in Allentown, PA. He has authored or coauthored more than 50 technical journal articles and conference presentations and a book chapter. His research interests include high-power diode lasers, compound semiconductor phase modulators, photonic integrated circuits, quantum cascade lasers, and visible III-nitride photonics. Dr. Siriani is a member of the Optical Society of America and IEEE/Photonics Society.

**Leo J. Missaggia** received the A.S. degree in mechanical engineering technology from Franklin Institute of Boston, the B.S. degree in mechanical engineering technology from Northeastern University in 1988, and the M.S. degree in mechanical engineering from Boston University in 1994. He joined Lincoln Laboratory, Massachusetts Institute of Technology, in 1980, and is currently an Associate Staff Member in the Laser Technology and Applications Group. His research interests include development of high-power semiconductor lasers and amplifiers, with a particular emphasis on advanced device packaging architectures including thermal management for high power CW operation, current distribution for individually addressable array emitters, and alignment and attachment of micro-optics and optical fibers. His work has resulted in coauthorships on several patents and numerous publications.

**Michael K. Connors** received the B.S. degree in biological science and environmental science from the University of Massachusetts Lowell in 1977. After graduation, he joined Lincoln Laboratory, Massachusetts Institute of Technology, where he is currently an Associate Staff Member in the Laser Technology and Applications Group. He is the author or coauthor of more than 75 publications. His research interests include development of device fabrication processes, reactive ion etching of semiconductor materials, and thin film deposition of dielectric and metal coatings.

**Tobias S. Mansuripur** received the B.Sc. degree in physics from University of California, Santa Barbara in 2009, the M.A.St. degree as a Churchill Scholar from Cambridge University in 2010, and the Ph.D. degree in physics from Harvard in 2016. His thesis work uncovered a new mode-locking mechanism in quantum cascade lasers. He is currently a Laser Scientist at Pendar Technologies, Cambridge, MA.

**Daniel R. Calawa,** photograph and biography not available at the time of publication.

**Daniel McNulty,** photograph and biography not available at the time of publication.

**Michael Nickerson** received the B.S. degree from the University of Washington in 2006. He joined Lincoln Laboratory in 2014, where he has been an Assistant Staff Member in the Laser Technology and Applications Group. His research interests include laser optics, precision measurement, data automation.

**Joseph P. Donnelly** (LF'05) received the Bachelor's degree from Manhattan College, Bronx, NY, and the M.S. and Ph.D. degrees from Carnegie Mellon University, Pittsburgh, PA, all in electrical engineering.

He is a Senior Staff Member in Lincoln Laboratory, Massachusetts Institute of Technology. Before joining Lincoln Laboratory, he was a NATO Postdoctoral Fellow at Imperial College, London, England. In addition to his position at Lincoln, he was until recently an Adjunct Professor in the Physics Department, University of Massachusetts Lowell. His current interests include high power semiconductor lasers, integrated optics and avalanche photodiodes.

Dr. Donnelly is a member of The Bohmesche Physical Society, Eta Kappa Nu and Sigma Xi. He was a National Lecturer for the IEEE Electron Devices Society in 1979. In 2001, he was a Guest Associate Editor for a special issue of the IEEE JOURNAL OF SELECTED TOPICS IN QUANTUM ELECTRONICS on semiconductor lasers and from 2002 to 2004 was an Associate Editor of the IEEE JOURNAL OF QUANTUM ELECTRONICS.

**Kevin Creedon** received the B.S. degree in electrical engineering from Villanova University in 2008. He is currently an Associate Staff Member in the Laser Technology and Applications Group, Lincoln Laboratory. His research interests include beam combining of semiconductor lasers and development of high-power fiber amplifiers.

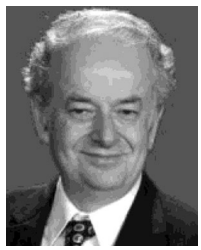

**Federico Capasso** is the Robert Wallace Professor of applied physics at Harvard University, which he joined in 2003 after 27 years at Bell Labs where his career advanced from Postdoctoral Fellow to Vice President for Physical Research. He and his group have made wide ranging contributions to optics, photonics, and nanotechnology, including pioneering the bandgap engineering technique, the invention of the quantum cascade laser, the first measurement of the repulsive Casimir force and more recently research on metasurfaces and their applications, including the generalized Snell's law and flat lenses. He is a member of the National Academy of Sciences, the National Academy of Engineering, the American Academy of Arts and Sciences (AAAS), the Academia Europaea and a foreign member of the Accademia dei Lincei. His awards include the Balzan Prize, the Rumford Prize of the American Academy of Arts and Sciences, the IEEE Edison Medal, the American Physical Society Arthur Schawlow Prize, the King Faisal Prize, the SPIE Gold Medal, the AAAS Rumford Prize, the IEEE Sarnoff Award, the Materials Research Society Medal, the Franklin Institute Wetherill Medal, the European Physical Society Quantum Electronics Prize, the Rank Prize in Optoelectronics, the Optical Society Wood Prize, the Berthold Leibinger Future Prize, the Julius Springer Prize in applied physics, the Institute of Physics Duddell Medal, the Jan Czochralski Award for lifetime achievements in materials science, and the Gold Medal of the President of Italy for meritorious achievement in science.